OPEN ACCESS

SIMULATION AND EXPERIMENTAL STUDY OF A DOUBLE-IMPACT HORIZONTAL ROTOR WAVE ENERGY GENERATOR

Zhongliang Meng[1,2], Yi Ding[3], Zijian Li[1]*
[1]College of Engineering, Qufu Normal University, Rizhao 276826, China
[2]Institute of Marine Science and Technology, Shandong University, Qingdao 266237, China
[3]School of Automation and Electrical Engineering, Zhejiang University of Science and Technology, Hangzhou 310023, China

Abstract - For sea areas characterized by low wave heights, short periods, and low energy flux densities, a double-impact horizontal rotor wave energy converter based on the involute principle was designed. A numerical model was established, and the rotor–wave impact process was investigated through numerical wave tank simulations. The simulation employed the VOF multiphase flow model to compare and analyze the rotational performance of rotors with different blade numbers. The results show that the rotor with 14 blades exhibits the optimal torque output characteristics. Experimental studies were carried out using a 1:2.5 scaled physical model in a wave flume. Under test conditions with wave heights of 0.1–0.12m and a wave period of 1.9s, the measured average torque ranged from 0.62 to 0.64N·m, and the average rotational speed reached 38.32–45.26r/min. The experiments verified the device's ability to operate stably under low energy flux conditions. The research results provide an effective technical solution for improving the efficiency of wave energy utilization.

Keywords: Wave energy generator, Horizontal rotor, Blades, Wave flume experiment.

1. Introduction

With the rapid development of the global industrial economy, the continuous growth in fossil energy consumption, coupled with the heavy reliance of industrial systems on petroleum, natural gas, and other resources, has posed an imminent risk of resource depletion [1, 2]. At present, there is an urgent need to gradually replace fossil fuels with clean energy sources. Covering 71% of the Earth's surface, the ocean harbors abundant renewable energy potential, yet less than 5% has been explored and utilized [3-5]. Ocean energy encompasses various forms, including wave energy, tidal energy, ocean thermal energy, and salinity gradient energy, among which wave energy demonstrates particularly significant development potential [6]. The widespread deployment of ocean monitoring equipment also demands stable and continuous power supply, further highlighting the necessity of wave energy exploitation.

Wave energy resources along the Chinese coast are characterized by relatively low wave heights, short periods, and low energy flux density, with effective wave heights ranging from 0.5-4 m and average periods of 4-6 s [7]. These values are significantly lower than those observed in high-energy seas such as the North Atlantic and South Pacific. As a result, the energy capture efficiency of most wave energy converters remains limited, hindering their large-scale commercialization [8]. Nevertheless, this resource characteristic simultaneously offers potential opportunities for specific technological approaches. To address this challenge, this study draws inspiration from hydro-turbine power generation principles and, based on the involute theory, proposes an innovative horizontal rotor structure [9, 10]. A numerical model of a double-impact horizontal rotor wave energy converter is established [10, 11]. By constructing a numerical wave tank and incorporating both wave-making and wave-absorbing methods, the rotational process of the horizontal rotor under wave excitation is simulated, thereby realizing the conversion of wave energy into mechanical energy for effective energy capture [9, 12]. In addition, a physical model was developed, and flume experiments were conducted to evaluate the start-up performance of the device under low wave height and short period sea conditions.

https://doi.org/10.17683/ijomam/issue22.v1.8

2. Principle of Operation

Based on the involute principle, this study designed the fundamental structure of a double-impact horizontal rotor. The device is composed of an inlet flow channel, a horizontal rotor, and an outlet flow channel. A sketch was established on the reference plane, and the involute blade profile was precisely drawn according to the dimensional parameters of the rotor's inner and outer diameters. The design principle is illustrated in Figure 1(a), and the rotor dimensions are listed in Table 1.

Table 1. Rotor size design table

Parameter	Symbol	Value
Outer diameter	D1	200/mm
Inner diameter	D2	130/mm
Base circle radius	R1	0.233D1/mm

Involute equation in (1):

$$\begin{cases} X = r \cdot \left(t \cdot \sin\left(t\right) + \cos\left(t\right) \right) \\ Y = r \cdot \left(\sin\left(t\right) - t \cdot \cos\left(t\right) \right) \end{cases} \quad (1)$$

In the equation, r denotes the base circle radius of the involute, and t represents the range of the involute extension angle.

When incident waves propagate to the rotor inlet, the initial wave impact induces a counterclockwise rotational motion of the horizontal rotor, while simultaneously causing the water level in the outlet channel to rise. During the wave backflow phase, the water level in the outlet channel decreases, and its potential energy is converted into kinetic energy, driving the rotor to rotate again in the counterclockwise direction. Thus, a complete motion cycle is accomplished.

This periodic motion continues until the subsequent wave impact occurs. The working principle is illustrated in Figure 1(b).

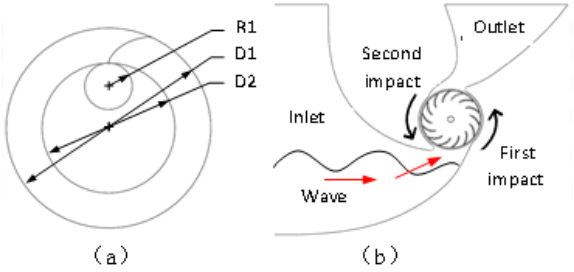

Figure 1: Design principles (a) Turbine Rotor, (b) Working principle

3. Numerical Simulation

- ***Mesh Generation***

In SpaceClaim, the imported model was pre-processed by performing region naming and Boolean operations for geometric segmentation [13-14]. In the Mesh module, the horizontal rotor region was refined, and boundary conditions were defined as follows: the numerical wave tank inlet was set as INLET, the outlet as OUTLET, the top surface as UP, and the outer wall of the impeller as fan-wall. The computational fluid domain was divided into three regions: the numerical wave tank domain (FLUID1), the flow channel domain (FLUID2), and the rotor rotational domain (FLUID3). Boundary layer mesh parameters were configured for the rotor wall, flow channel wall, and outer flow field wall surfaces. The updated mesh is shown in Figure 2(a).

The design parameters of the numerical wave tank and the wave generation conditions are listed in Table 2. The horizontal rotor was positioned 4 m away from the wave tank inlet, as illustrated in Figure 2(b). The total length of the tank was 20 m, with a free surface elevation of 1 m and a total water depth of 2 m. The wave propagation effect is depicted in Figure 2(c).

Table 2. Rotor size design

Parameter	Tank length(m)	Tank width(m)	Tank height(m)	Wave height(m)	Wavelength (m)	Wave period(s)
Value	20	2	3	0.2	4	2

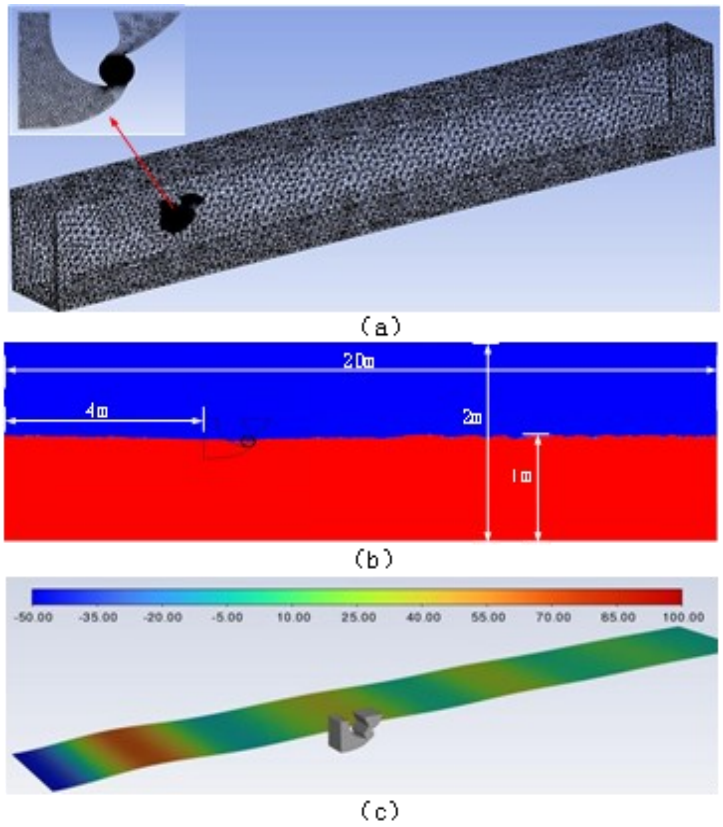

Figure 2: Numerical Simulation (a) Flow channel mesh division (b) Numerical model position; (c) Simulation results

- ***Numerical Wave Tank Simulation Method***

In the solver settings, a transient solution method was adopted, and the standard gravitational acceleration in the negative Y-direction was applied [15, 16]. The Volume of Fluid (VOF) method in the multiphase flow model was selected, with the implicit scheme and the implicit body force option enabled. To accurately reproduce wave tank conditions, the open-channel wave generation module of the VOF model was activated. For material properties, air was defined as the primary phase fluid and water as the secondary phase fluid. The surface tension coefficient of water was set to 0.07 N/m. The three-dimensional Navier-Stokes (N-S) differential equations consist of the continuity equation and the momentum equation, expressed as follows:

Continuity equation in (2):

$$\frac{\partial \rho}{\partial t}+\frac{\partial(\rho u)}{\partial x}+\frac{\partial(\rho v)}{\partial y}+\frac{\partial(\rho w)}{\partial z}=0 \tag{2}$$

For incompressible fluids, the momentum equation can be expressed as (3):

$$\frac{\partial u}{\partial x}+\frac{\partial v}{\partial y}+\frac{\partial w}{\partial z}=0 \tag{3}$$

In the equations: ρ denotes the fluid density, and u,v,w represents the x,y,z directional component.

The momentum equations can be expressed as follows:

In the x-direction in in (4):

$$\rho\left(\frac{\partial u}{\partial t}+u\frac{\partial u}{\partial x}+v\frac{\partial u}{\partial y}+w\frac{\partial u}{\partial z}\right)=-\frac{\partial p}{\partial x}+\mu\left(\frac{\partial^2 u}{\partial x^2}+\frac{\partial^2 u}{\partial y^2}+\frac{\partial^2 u}{\partial z^2}\right)+f_x \tag{4}$$

In the y-direction in (5):

$$\rho\left(\frac{\partial v}{\partial t}+u\frac{\partial v}{\partial x}+v\frac{\partial v}{\partial y}+w\frac{\partial v}{\partial z}\right)=-\frac{\partial p}{\partial y}+\mu\left(9\frac{\partial^2 v}{\partial x^2}+\frac{\partial^2 v}{\partial y^2}+\frac{\partial^2 v}{\partial z^2}\right)+f_y \tag{5}$$

In the z-direction in (6):

$$\rho\left(\frac{\partial w}{\partial t}+u\frac{\partial w}{\partial x}+v\frac{\partial w}{\partial y}+w\frac{\partial w}{\partial z}\right)=-\frac{\partial p}{\partial z}+\mu\left(\frac{\partial^2 w}{\partial x^2}+\frac{\partial^2 w}{\partial y^2}+\frac{\partial^2 w}{\partial z^2}\right)+f_z+P\mathrm{g} \tag{6}$$

The vector form is given as in (7):

$$\rho\left(\frac{\partial u}{\partial t}+u\cdot\nabla u\right)=-\nabla P+\mu\nabla^2 u+f \qquad (7)$$

Where P denotes the pressure, μ represents the dynamic viscosity, and $f=\left(f_x,f_y,f_z\right)$ refers to the body force.

The VOF model simulates multiphase flow motion by solving the continuity and momentum equations.

Continuity equation in (8):

$$\frac{\partial\rho}{\partial t}+\nabla\cdot\left(\rho u\right)=0 \qquad (8)$$

Where ρ denotes the mixture density and u represents the velocity vector.

Momentum equation in (9):

$$\frac{\partial(\rho u)}{\partial t}+\nabla\cdot\left(\rho uu\right)=-\nabla P+\nabla\cdot\left[\mu\left(\nabla u+\nabla u^T\right)\right]+P\mathrm{g}+F_{st} \qquad (9)$$

Where P denotes the pressure, μ represents the mixture dynamic viscosity, g is the gravitational acceleration, and F_{st} refers to the surface tension.

Volume fraction equation in (10):

$$\frac{\partial c_2}{\partial c_2}+\nabla\cdot\left(a_i u\right)=0 \qquad (10)$$

This equation is used to track the volume fraction of each fluid.

For turbulence modeling, the turbulence model was adopted due to its excellent capability in predicting shear stresses and its broad applicability, which allows accurate simulation of boundary layer flow characteristics.

The model was adopted due to its excellent capability in predicting shear stresses and its broad applicability, which allows accurate simulation of boundary layer flow characteristics.

The model consists of two transport equations:

Turbulent kinetic energy equation in (11):

$$\frac{\partial\left(\rho k\right)}{\partial t}+\frac{\partial\left(\rho u_j k\right)}{\partial x_j}=P_k-\beta^*\rho\omega k+\frac{\partial}{\partial x_j}\left[\left(\mu+\sigma_k u_t\right)\frac{\partial_k}{\partial x_j}\right] \qquad (11)$$

Turbulent dissipation rate equation in (12):

$$\frac{\partial\left(\rho\omega\right)}{\partial t}+\frac{\partial\left(\rho u_j\omega\right)}{\partial x_j}=a\frac{\omega}{k}P_k-\beta\rho\omega^2+\frac{\partial}{\partial x_j}\left[\left(\mu+\sigma_\omega\mu_t\right)\frac{\partial\omega}{\partial x_j}\right]+2\left(1-F_1\right)\rho\sigma_{\omega^2}\frac{1\partial k\partial\omega}{\omega\partial x_j\partial x_j} \qquad (12)$$

Where ρ denotes the fluid density, k represents the turbulent kinetic energy, ω is the turbulent dissipation rate, u_j refers to the velocity component, P_k denotes the turbulent kinetic energy production term, μ is the dynamic viscosity, μ_t represents the turbulent viscosity, β^*, a, β, σ_k, σ_w is the model constant, and F_1 is the blending function used to switch between model k - ω and model k - ε.

- ***Inlet and Outlet Boundary Condition Settings***

In the boundary condition settings, the inlet of the external flow field was defined as an open-channel velocity inlet boundary condition, which can be expressed as (13):

$$\begin{aligned}u\left(t,y\right)&=U_0+u'\left(t,y\right)\\ v\left(t,y\right)&=0\\ w\left(t,y\right)&=0\end{aligned} \qquad (13)$$

Where $u\left(t,y\right)$ denotes the horizontal velocity component, which is a function of time t and vertical position y; U_0 represents the mean velocity; $u'\left(t,y\right)$ is the velocity fluctuation component; $v\left(t,y\right)$ and $w\left(t,y\right)$ refers to the vertical and lateral velocity components, which are usually set to zero.

The boundary conditions were set as follows: the upper interface and outlet of the external flow field were defined as pressure outlet boundary conditions, while the remaining surfaces were specified as wall boundaries. The inlet boundary was configured with the open-channel flow option, with the following parameters: an inlet mean velocity of 2 m/s, adoption of the intermediate shallow-water wave model, an initial free surface elevation of 1.36 m (below the horizontal rotor), and a bottom elevation of -1.5 m. The wave parameters included a period of 2 s, a wavelength of 4 m, a wave height of 0.2 m, and a wave incident angle of 120°. The free surface elevation and bottom elevation were set to be consistent at both the inlet and outlet boundaries. The wave simulation was conducted based on the second-order Stokes wave theory.

The wave profile of the second-order Stokes wave is expressed as (14):

$$\eta\left(x,y\right)=\frac{H}{2}\cos\left(kx-\omega t\right)+\frac{kH^2}{16}\frac{\cosh\left(kh\right)}{\sinh^3\left(kh\right)}\left[2+\cosh\left(2kh\right)\right]\cos\left(2\left(kx-\omega t\right)\right) \qquad (14)$$

Where H denotes the wave height, k is the wave number($k = \frac{2\pi}{\lambda}$; λ is the wavelength); ω represents the angular frequency; h is the water depth; x is the horizontal coordinate; and t denotes the time.

The surface horizontal and vertical velocities are given as (15):

$$\begin{aligned} u(x,z,t) &= \frac{H}{2}\omega\frac{\cosh(k(z+h))}{\sinh(kh)}\cos(kx-\omega t)+\frac{3}{16}H^2\omega k\frac{\cosh(2k(z+h))}{\sinh^4(kh)}\cos(2(kx-\omega t)) \\ w(x,z,t) &= \frac{H}{2}\omega\frac{\sinh(k(z+h))}{\sinh(kh)}\sin(kx-\omega t)+\frac{3}{16}H^2\omega k\frac{\sinh(2k(z+h))}{\sinh^4(kh)}\sin(2(kx-\omega t)) \end{aligned} \quad (15)$$

The pressure distribution $p(x,z,t)$ can be expressed as (16):

$$p(x,z,t) = -\rho g z + \rho g\frac{H}{2}\frac{cosh(k(z+h))}{cosh(kh)}cos(kx-\omega t)+\frac{1}{4}\rho g H^2 k\frac{cosh(2k(z+h))}{sinh(2kh)}cos(2(kx-\omega t)) \quad (16)$$

Where ρ denotes the fluid density and g the gravitational acceleration.

In the FLUID1 computational domain, a numerical wave-damping function was configured as follows: the numerical beach model was activated at the numerical wave tank inlet (INLET) to create distinct wave-generation and wave-absorption zones, thereby reproducing the wave-making and energy-dissipation processes of a physical wave flume.

- ***Adaptive Mesh Settings***

Adaptive mesh refinement (AMR) dynamically adjusts mesh density according to the spatial gradients of the physical fields, geometric features, and intermediate solution outputs. Mesh is refined in key regions to enhance solution accuracy and coarsened in non-critical areas to optimize computational resource allocation. The specific mechanisms are as follows: (i) gradient-based adaptation, which refines the mesh in regions with pronounced interfacial or field gradients; (ii) geometry-aware adaptation, which applies differentiated refinement according to geometric complexity; and (iii) solution-driven optimization, which adjusts mesh resolution based on the distribution of numerical errors.

Equation for gradient-based refinement.

Gradient criterion: if the magnitude of the gradient of a physical quantity ϕ exceeds a prescribed threshold, the mesh is refined in (17):

$$\left|\nabla^2\phi\right| \geq \in_{gradient} \quad (17)$$

Where $\in_{gradient}$ is the threshold.

Curvature criterion: used to refine the mesh in geometrically curved regions in (18).

$$k = \frac{\left|\nabla^2\phi\right|}{\left(1+\left|\nabla\phi\right|^2\right)^{\frac{3}{2}}} \geq \in_{curvature} \quad (18)$$

Where k denotes the curvature.

In the computational domain, the seawater region was tagged and locally initialized, and the interfacial gradient threshold was set to 10. For seawater regions where the gradient exceeds the threshold, adaptive mesh refinement (AMR) was enabled with a refinement level of 2 and a minimum of 3 refinement layers. A transient solver was employed with a time step of 0.01 s; 10 iterations were performed per time step, with the maximum number of iterations capped at 20.

- ***Dynamic Mesh Parameter Settings***

The mesh smoothing and remeshing algorithms were enabled, and the six-degrees-of-freedom (6-DOF) solver module was activated. For the dynamic mesh region “fan”, the following parameters were configured: the mass properties (including mass, moments of inertia, centroid coordinates, and rotation-axis location) were assigned based on the SolidWorks model; the rotor wall was defined as a rigid-body motion type and a minimum cell size was specified. The same “fan” attributes were applied to the rotating domain, and passive rotation mode was enabled to synchronize the motion of the rotating domain with that of the rotor wall.

- ***Solution Setup***

The SIMPLE algorithm was employed. The momentum equations were discretized using a second-order upwind scheme, and the pressure term was discretized using the PRESTO! scheme. During initialization, standard initialization was applied at the INLET boundary, and the open-channel inlet was initialized using the FLAT mode. An XY-plane section was created for post-processing visualization to display the distributions of the density, pressure, and velocity fields, thereby characterizing the wave–rotor interaction process. The computational parameters were set as follows: time step 0.01 s, total of 1000 time steps, and a maximum of 20 iterations per time step.

4. Simulation Results and Analysis

Figure 3 illustrates the dynamic impact process of the double-impact horizontal-rotor wave energy converter. Based on the simulation results, a 14-blade double-impact involute horizontal rotor was selected as the test article. Taking t = 5 s as the initial time, a complete cycle is analyzed as follows. When the incident wave strikes the rotor, passive rotation is initiated and the water level in the outlet channel rises; at this stage, the torque increases and the rotational speed accelerates, completing the first impact on the rotor during the wave-inflow phase. In the 5.0-5.2 s phase, the wave fully submerges the rotor domain, the torque reaches its peak, and the growth rate of rotational speed increases markedly, completing the second impact on the rotor during the wave-inflow phase. By 6.2 s, the wave injection into the outlet channel is completed, the water level stabilizes at a mid-level, and the discharge process begins. During 6.2-6.4 s, the falling water level causes the torque to climb to a second peak and the rotational speed continues to rise, completing the first impact on the rotor during the wave-outflow phase.

From 6.4-6.6 s, the rotational speed attains its maximum; from 6.6-6.8 s, the rotational speed decays and the torque drops to a trough at 6.8 s, completing the second impact on the rotor during the wave-outflow phase. By 7.4 s, the channel is completely drained, the torque fluctuates around zero, and the time interval between two successive wave impacts on the rotor is defined as the wave preparation stage.

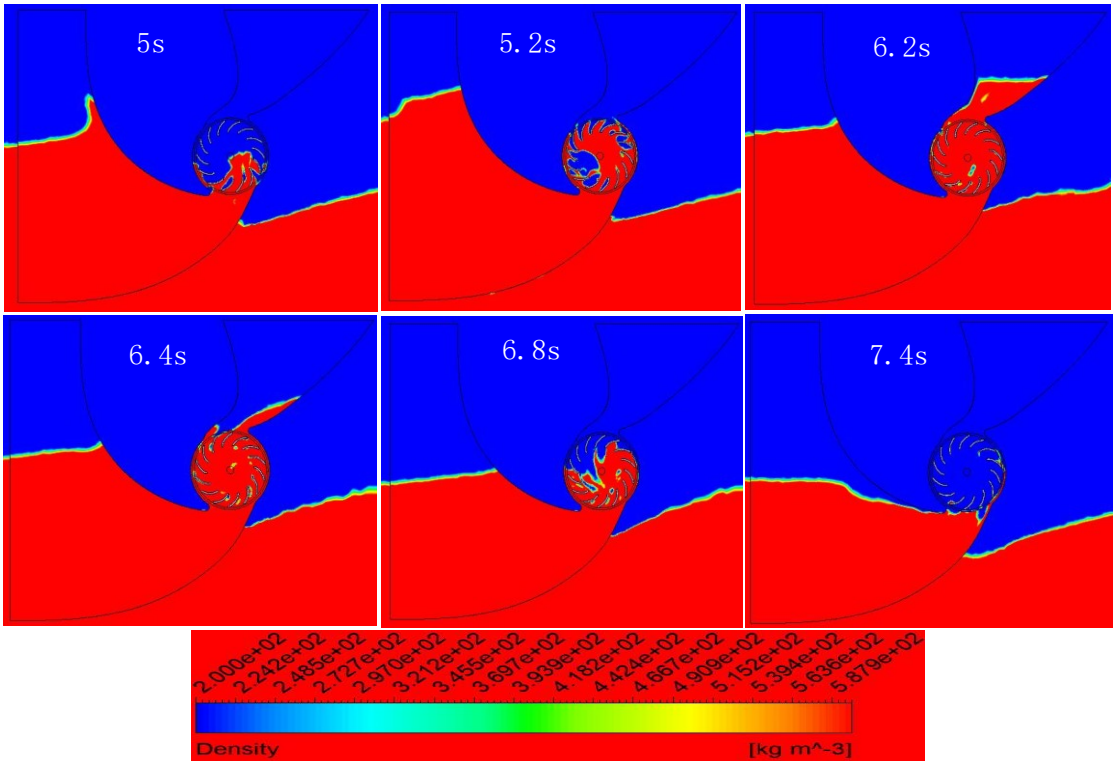

Figure 3: Density cloud map of water turbine

Due to the structural characteristics of the double-impact horizontal-rotor wave energy converter, a high-pressure impact zone forms at the bottom of the inlet channel, where the resulting pressure gradient promotes flow convergence and impingement on the horizontal rotor; by contrast, the channel top and the outlet channel remain at low pressure because they are open to the atmosphere. The lower blades of the rotor experience localized high-pressure regions under the wave-impact loading from the bottom channel, thereby driving blade rotation. When the fluid enters the impeller region, the lower blades near the inlet channel exhibit a pronounced high-pressure area whose spatial distribution and magnitude vary with the number of blades, indicating that blade count directly determines the device's energy conversion efficiency by modulating the pressure field.

As shown by the pressure contours in Figure 4, the blade-surface pressure distributions differ markedly among rotors with different blade numbers.

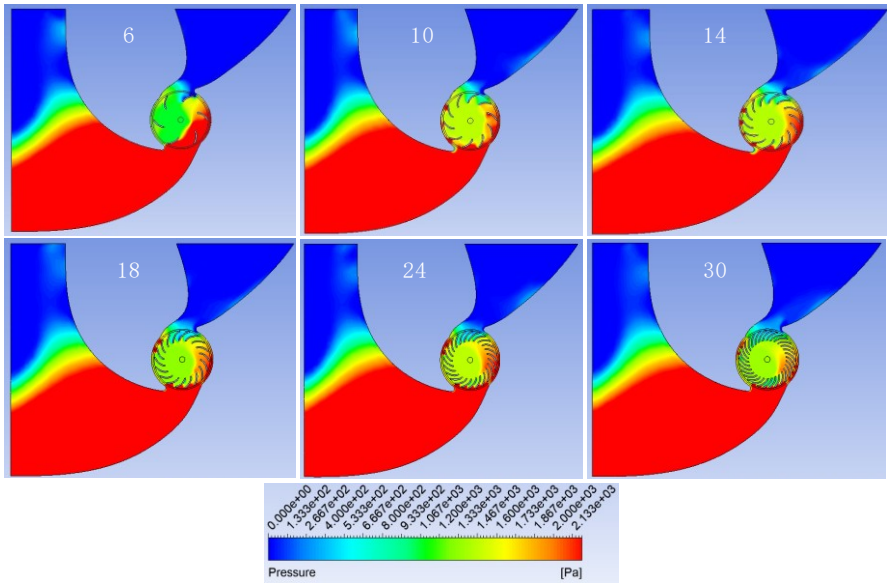

Figure 4: Cloud map of turbine pressure

As shown in Figure 5(a), the torque and rotational speed of rotors with different blade counts indicate that the 14-blade rotor exhibits the most favorable dynamic response. In the initial stage, the torque rises rapidly to a peak and then gradually decays. Under subsequent periodic wave loading, the torque response displays a typical alternating positive-negative pattern and approaches a steady state. Comparative analysis shows that this configuration achieves a markedly higher peak torque than the other blade counts, maintains superior periodic torque peaks, and delivers the best overall torque-output performance.

The rotational-speed characteristics reveal a periodic accelerate-decelerate behavior for all rotors: the 10-blade rotor attains the highest initial speed, followed by the 6- and 14-blade rotors. A comprehensive assessment indicates that the 14-blade rotor sustains a relatively high peak speed while offering the best operational stability (lowest decay rate after 6 s). By contrast, the 6- and 10-blade rotors decay too rapidly, and the 18-30-blade rotors suffer from inadequate start-up performance due to excessive rotational inertia. Accordingly, the 14-blade rotor is identified as the optimal design.

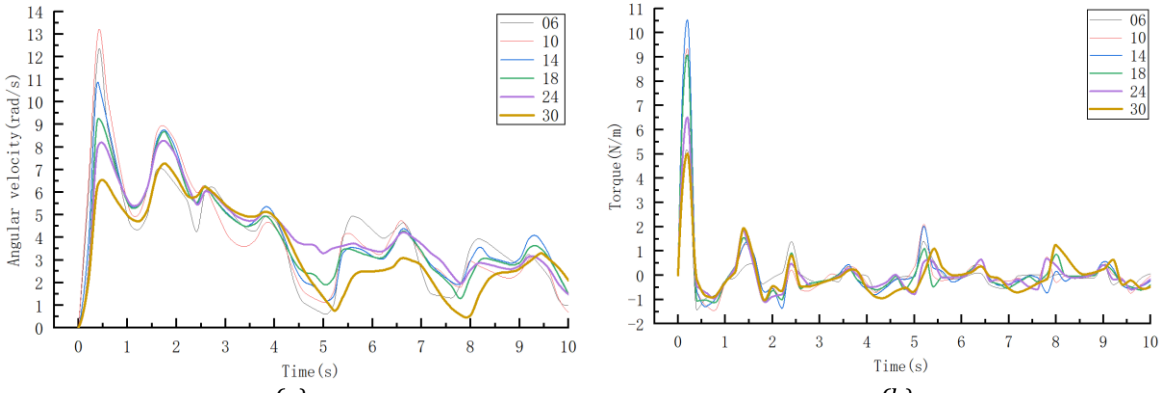

(a) *(b)*

Figure 5: Horizontal rotor torque and speed variation (a) Torque; (b) Rotational speed

5. Flume Experiments

The novel horizontal-rotor, direct-drive wave energy converter designed in this study has a prototype rated capacity of 6 kW, a total mass of 28 t, and overall dimensions of $6m \times 6m \times 5.4m(L \times W \times H)$. A physical model was fabricated at a 1:2.5 scale, with dimensions of $1.1m \times 1.0m \times 1.8m$. The experiments were conducted in a flume measuring $30m \times 4m \times 3m(L \times W \times H)$.

The model was installed 10 m from the wavemaker, hoisted by an overhead crane and secured using bottom ballast weights. Under regular wave conditions, the rotor rotational speed and torque sensor data were monitored to analyze the start-up characteristics and to investigate the variation of drivetrain torque at different rotational speeds [9]. The specific parameters are listed in Table 3, and the experimental setup is shown in Figure 6.

Table 3. Experimental conditions

Experimental Conditions	Sea-State Parameters		Experimental Parameters	
Test Conditions	Wave Height H (m)	Wave Period T (s)	Wave Height H (m)	Wave Period T (s)
Test Conditions 1	0.25	3	0.10	1.9
Test Conditions 2	0.30	3	0.12	1.9

Figure 6: Flume experiments

Figure 7(a) presents the time histories of rotor torque and rotational speed under Case 1: with a wave period of 1.9 s and a wave height of 0.10 m, the measured mean torque was 0.62 N·m and the mean rotational speed was 38.32 r/min, indicating stable generator operation. Figure 7(b) shows the corresponding results for Case 2: when the wave period was kept at 1.9 s and the wave height increased to 0.12 m, the mean torque rose slightly to 0.64 N·m, while the mean rotational speed increased markedly to 45.26 r/min; the generator continued to operate normally. Comparative analysis indicates that the difference in mean torque between the two cases is small, whereas Case 2 exhibits a significant increase in mean rotational speed. Under low-wave-height (0.10-0.12 m) and short-period (1.9 s) sea states, the device demonstrates excellent start-up performance.

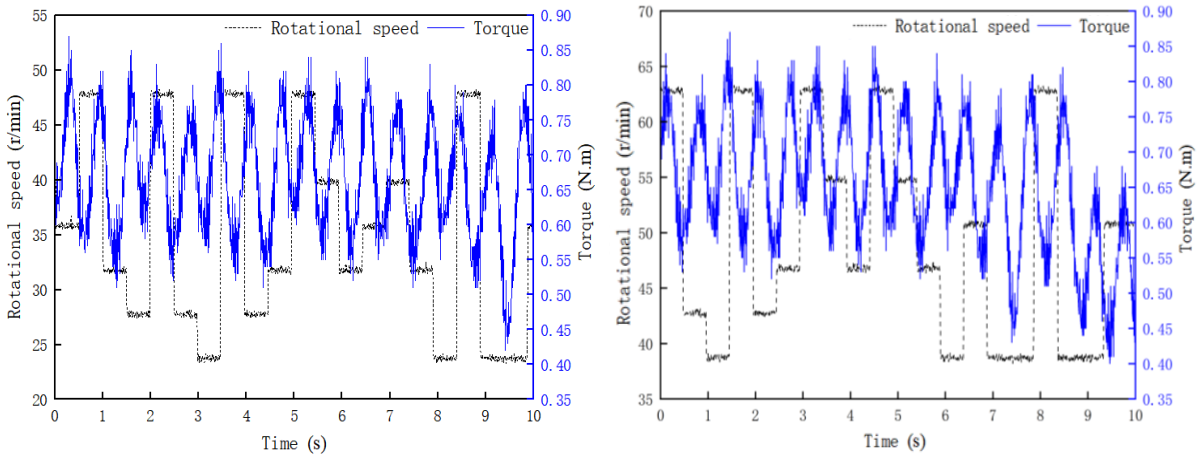

(a) *(b)*

Figure7: Changes in speed and torque (a) Condition 1; (b) Condition 2

6. Conclusions

Considering the characteristics of wave energy resources along the Chinese coast-effective wave heights of 0.5-4 m, periods of 4-6 s, and low energy-flux density-this study proposes a novel double-impact horizontal-rotor wave energy converter based on the involute principle to enhance energy capture under low-energy-density sea states. Numerical model was developed, and a numerical wave tank was constructed using the VOF multiphase model coupled with the SST$-\omega$ turbulence model to simulate the wave-rotor interaction and to verify the conversion mechanism from wave energy to mechanical energy. Simulation analyses for 6-30 blade counts identified the 14-blade rotor as optimal under conditions of wave height 0.2 m, period 2 s, and wavelength 4 m, delivering superior peak torque and stability relative to the other configurations. Guided by these results, a 1:2.5-scale physical model was fabricated and tested in a 30 m flume. The experiments show that, under 0.10-0.12 m wave height and 1.9 s wave period, the device exhibits good start-up performance, with mean torque 0.62-0.64 N·m and mean rotational speed 38.32-45.26 r/min, while maintaining stable generator operation.

By combining numerical simulation with physical experiments, this work identifies the optimum rotor configuration and provides an innovative solution for efficient wave-energy exploitation along the Chinese coast. Future research will focus on structural optimization and cost reduction, and will explore multi-energy hybridization pathways to promote commercialization in scenarios such as island power supply.

Acknowledgment

This research was funded by Shandong Provincial Natural Science Foundation (Grant No. ZR2024ME241).

References

[1] P. Chen, D. Wu, A review of hybrid wave -tidal energy conversion technology, Ocean Eng 303(2024).

[2] M. Shalby, D.G. Dorrell, P. Walker, Multi-chamber oscillating water column wave energy converters and air turbines: A review, Int J Energ Res 43(2)(2019) 681-696.

[3] C. Li, L. Xu, L. Zhu, S. Zou, Q.H. Liu, Z. Wang, H. Chen, Concentrators for Water Waves, Phys Rev Lett 121(10)(2018).

[4] A.F.O. Falcao, J.C.C. Henriques, Oscillating-water-column wave energy converters and air turbines: A review, Renew Energ 85(2016) 1391-1424.

[5] M. Melikoglu, Current status and future of ocean energy sources: A global review, Ocean Eng 148(2018) 563-573.

[6] A.G.L. Borthwick, Marine Renewable Energy Seascape, Engineering 2(1)(2016) 69-78.

[7] T. Aderinto, H. Li, Ocean Wave Energy Converters: Status and Challenges, Energies 11(5)(2018) 1250.

[8] E. Segura, R. Morales, J.A. Somolinos, A strategic analysis of tidal current energy conversion systems in the European Union, Appl Energ 212(2018) 527-551.

[9] Z. Meng, Y. Chen, S. Li, The Shape Optimization and Experimental Research of Heave Plate Applied to the New Wave Energy Converter, Energies 15(4)(2022) 1313.Z. Meng, Y. Ding, Y. Chen, S. Li, Experimental study on heave performance of a new wave energy power generation device based on regular waves, Ocean Eng 252(2022) 111099.

[10] T. Yu, Q. Guo, H. Shi, T. Li, X. Meng, S. He, P. Li, Experimental investigation of a novel OWC wave energy converter, Ocean Eng 257(2022) 111567.

[11] F. Huang, P. Yang, Z. Liu, D. Yang, L. Huang, Y. Shi, X. Tao, Y. Chen, H. Li, X. Chen, Z. Bian, A hybrid nanogenerator for collecting both water wave and steam evaporation energy, Nano Energy 110(2023) 108346.

[12] P. Halder, S. Nagata. Numerical Analysis of a Floating Body Pendulum Wave Energy Converter Using Vortex Method.: IEEE 2022. p. 1-6.

[13] M. Jafari, A. Babajani, P. Hafezisefat, M. Mirhosseini, A. Rezania, L. Rosendahl, Numerical simulation of a novel ocean wave energy converter, Energy Procedia 147(2018) 474-481.

[14] M.A. Zullah, Y. Lee, Performance evaluation of a direct drive wave energy converter using CFD, Renew Energ 49(2013) 237-241.

[15] W. Lai, Y. Xie, D. Li, Numerical Study on the Optimization of Hydrodynamic Performance of Oscillating Buoy Wave Energy Converter, Pol Marit Res 28(1)(2021) 48-58.